

# Probing the Fermi surface with Quantum Oscillation Measurements in the Dirac semimetal TaNiTe<sub>5</sub>

Maximilian Daschner,<sup>\*</sup> F. Malte Grosche, and Cheng Liu  
*Cavendish Laboratory, University of Cambridge, Cambridge CB3 0HE, United Kingdom*

Bruno Gudac and Mario Novak  
*Department of Physics, Faculty of Science, University of Zagreb, Zagreb, Croatia*

Ivan Kokanović<sup>†</sup>  
*Department of Physics, Faculty of Science, University of Zagreb, Zagreb, Croatia and  
Cavendish Laboratory, University of Cambridge, Cambridge CB3 0HE, United Kingdom*

(Dated: March 20, 2024)

We report a detailed investigation of the Fermi surface in the layered Dirac semimetal TaNiTe<sub>5</sub>, which hosts quasi-one-dimensional (quasi-1D) topological electronic properties. We have investigated the magnetoresistance and magnetic behaviour in high-quality TaNiTe<sub>5</sub> single crystals. Pronounced Shubnikov-de Haas (SdH) and de Haas-van Alphen (dHvA) oscillations are observed in magnetic fields above 3 T and at temperatures of up to 22 K. Five fundamental frequencies and light effective quasiparticle masses are obtained by fast Fourier transformation (FFT) and Lifshitz-Kosevich (LK) formula fits. The high resolution of the low-temperature FFT spectra allows us to investigate individual peaks in detail for the magnetic fields applied along all three crystallographic axes and in the  $a$ - $c$  plane. The extracted values for the Berry phase of the obtained Fermi pockets approach  $\pi$ , demonstrating the nontrivial topological electronic properties of layered TaNiTe<sub>5</sub>. The observed quantum oscillations in the magnetoresistance and magnetization data are consistent with ultra-high mobility Dirac carriers in the conduction band.

## I. INTRODUCTION

Topological semimetals represent a new class of quantum materials hosting Dirac [1–4] or Weyl fermions [5–13], in which the valence and conduction bands touch and form nodes. Furthermore, Dirac nodal-lines in which Dirac cones form lines in reciprocal space lead to the more general concept of nodal-line semimetals (NLSMs) [14–20]. NLSMs usually occur in three-dimensional materials where they hold more symmetries such as mirror and nonsymmorphic symmetries that protect the Dirac band touching structures against spin-orbit coupling (SOC) [16, 19]. Evidence for robust Dirac nodal lines in (quasi) one-dimensional materials has been missing until recently when they were reported in the exfoliatable, in-plane anisotropic nonmagnetic semimetal TaNiTe<sub>5</sub> by combining angle-resolved photoemission spectroscopy (ARPES) and density functional

theory (DFT) calculations [21]. Quantum oscillation studies have reported evidence for Fermi surface pockets with nontrivial Berry phase in TaNiTe<sub>5</sub>, and highly anisotropic properties were shown in magnetization and transport measurements [22–24]. These previous studies were performed for magnetic fields applied parallel to the crystallographic  $a$  and  $b$  axes. However, a systematic study of quantum oscillations for magnetic fields parallel to the crystallographic  $c$  axis or in the  $a$ - $c$  plane remains absent.

Here, we report a detailed investigation of the Fermi surface in TaNiTe<sub>5</sub> single crystals through magnetoresistance and magnetization measurements for magnetic fields of up to 14 T along all three principal axes and a rotational study in the  $a$ - $c$  plane. Three single crystals from the same batch are used for the resistance and magnetization measurements. We have observed pronounced de Haas-van Alphen (dHvA) and Shubnikov-de Haas (SdH) oscillations with multiple frequencies at temperatures below 22 K and magnetic fields above 3 T. The observed quantum oscillation frequencies in these crystals closely agree with each other, evidencing the same electronic structure.

---

<sup>\*</sup> md867@cam.ac.uk

<sup>†</sup> kivan@phy.hr

Changing the magnetic field direction results in a clear change of the oscillation frequencies, indicating anisotropic Fermi surface pockets. By analysing the SdH and dHvA quantum oscillations, multiple fundamental frequencies, small effective masses, low Dingle temperatures, and high mobility of charge carriers are obtained with the use of fast Fourier transformation (FFT) and Lifshitz-Kosevich (LK) formula fitting. The high resolution of the low-temperature FFT spectra in the observed magnetization and magnetoresistance data allows us to investigate individual peaks in detail for the magnetic fields applied along all three crystallographic axes and in the  $a$ - $c$  plane. The obtained values of the Berry phase for the Fermi pockets approach  $\pi$ , demonstrating the non-trivial topological electronic properties of layered TaNiTe<sub>5</sub>. These results suggest that the Dirac semimetal TaNiTe<sub>5</sub> represents a new platform in which to study the properties in quantum materials that host quasi-1D nontrivial topological electronic properties.

## II. EXPERIMENTAL METHODS

The TaNiTe<sub>5</sub> crystals were synthesized by the self-flux method [23, 25]. The molar ratio of elements was Ta:Ni:Te = 1:1:10. The mixture was loaded into an alumina crucible and sealed inside a quartz tube in high vacuum. The mixture was then heated to 700°C over the course of four days and then slowly cooled to 500°C within a week. The resulting single crystals have an orthorhombic layered structure with the space group Cmc<sub>2</sub>m (No. 63) [25]. The structure features one-dimensional (1D) NiTe<sub>2</sub> chains along the crystallographic  $a$  axis, which form a quasi-2D layer by linking chains of Ta atoms along the  $c$  axis as can be seen in Figure 6. The lattice constants are inferred from powder X-ray diffraction (XRD) data with  $a = 3.657 \text{ \AA}$ ,  $b = 13.183 \text{ \AA}$ , and  $c = 15.119 \text{ \AA}$  (See Figure 6). The peaks of the single-crystal XRD pattern showed no trace of an impurity phase, indicating high crystalline quality. The crystals grow in the shape of needles along the  $a$  axis. Magnetization measurements in two crystals of masses 25 mg and 27.4 mg were carried out using a 14 Tesla PPMS with VSM option. The magnetoresistance was measured using standard AC lock-in techniques on a 9 Tesla Quantum Design Physical

Property Measurement System (PPMS).

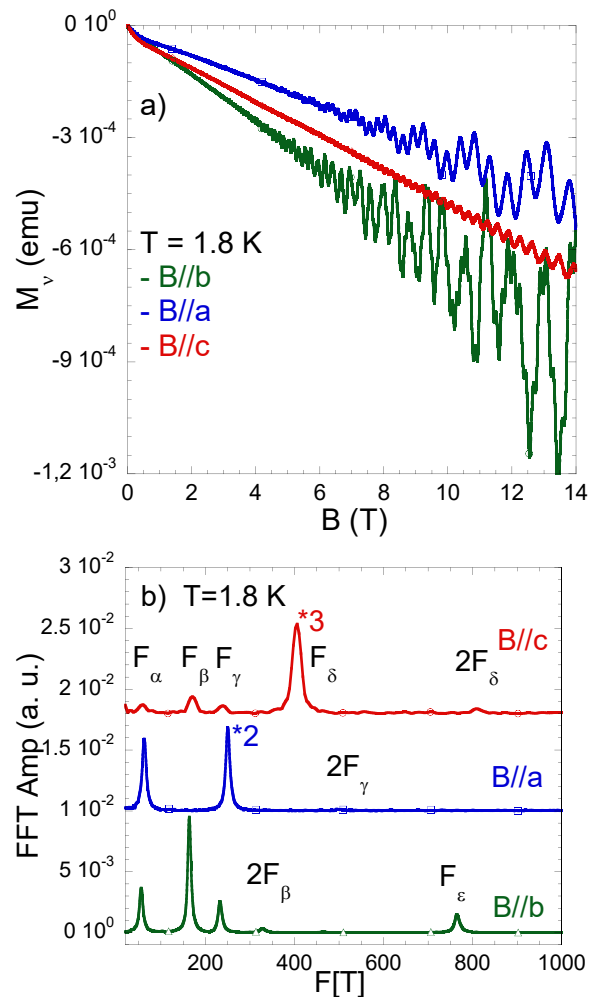


Figure 1. a) Magnetic field sweeps of the magnetization up to 14T of a layered TaNiTe<sub>5</sub> single crystal with a mass of 25.6 mg at a temperature of 1.8K. The magnetic fields are applied parallel to the crystallographic  $b$ ,  $a$ , and  $c$  axes, respectively. b) The FFT spectra of the oscillatory components of the dHvA oscillations of the isothermal magnetization data extracted by subtraction of the diamagnetic backgrounds shown in a). The FFT amplitudes of the spectra have been generated from the magnetization data between 4 and 14T. The curves show an interpolation of data points with a few data points highlighted for B|| $c$  (red circle), B|| $a$  (blue square), and B|| $b$  (green triangle). The FFT spectra are shifted vertically for clarity.

### III. EXPERIMENTAL RESULTS

#### A. Magnetization

Figure 1 a) shows a series of magnetic field sweeps of the magnetization up to 14T in TaNiTe<sub>5</sub> at a temperature 1.8K, with magnetic fields applied along the crystallographic *a*, *b*, and *c* axes. TaNiTe<sub>5</sub> exhibits large dHvA quantum oscillations with multiple frequencies superimposed on different linear diamagnetic backgrounds. By changing the direction of the magnetic field from  $\mathbf{B} \parallel b$  to  $\mathbf{B} \parallel a$ , and to  $\mathbf{B} \parallel c$ , the oscillation components are gradually suppressed, illustrating the anisotropic electronic properties of this material.

In Figure 1 b), we have performed an FFT analysis of the isothermal magnetization data shown in Figure 1 a). Several clearly resolved peaks are visible for the magnetic field parallel to the *b* axis, which we label as  $\alpha$ ,  $\beta$ ,  $\gamma$  and  $\varepsilon$  respectively. The observed frequencies ( $F$ ) in the FFT spectra are related to the extremal area  $A_F$  of the individual pockets via the Onsager relation  $F = A_F(\phi_0/2\pi^2)$ , where  $\phi_0$  is the magnetic flux quantum [26]. One main result of this work is the observation of two new frequencies at  $F_\gamma = 233\text{T}$  and  $F_\varepsilon = 766\text{T}$  for  $\mathbf{B} \parallel b$ . The other main result is the measurement of quantum oscillations in the direction of  $\mathbf{B} \parallel c$  where we find the new frequency  $F_\delta = 405\text{T}$ . The other frequencies we found are consistent with the literature [22–24]. The magnetic field sweeps of the magnetization up to 14T on a TaNiTe<sub>5</sub> single crystal at various temperatures between 1.8 and 22K with the magnetic field applied parallel to all three crystallographic axes are given in the appendix. In the following we will analyse the quantum oscillations in the magnetization, and explore their topologically non-trivial properties.

In metals and semimetals, oscillations in the magnetization are well described by the Lifshitz-Kosevich (LK) formula [26]:

$$\Delta M = AB^{1/2}R_T R_D \sin \left[ 2\pi \left( \frac{F}{B} + (1/2 - \phi) \right) \right] \quad (1)$$

where  $A$  is a constant,  $R_T = X/(\sinh X)$  with  $X = 2\pi^2 k_B m^* T / (\hbar e B)$  is the temperature damping factor,  $R_D = \exp(XT_D/T)$  is the Dingle damping factor,  $F$  is the dHvA frequency of the oscillations, corresponding to an extremal area of the Fermi surface perpendicular to the magnetic field  $B$ , and  $m^*$  is the quasiparticle effective mass. We

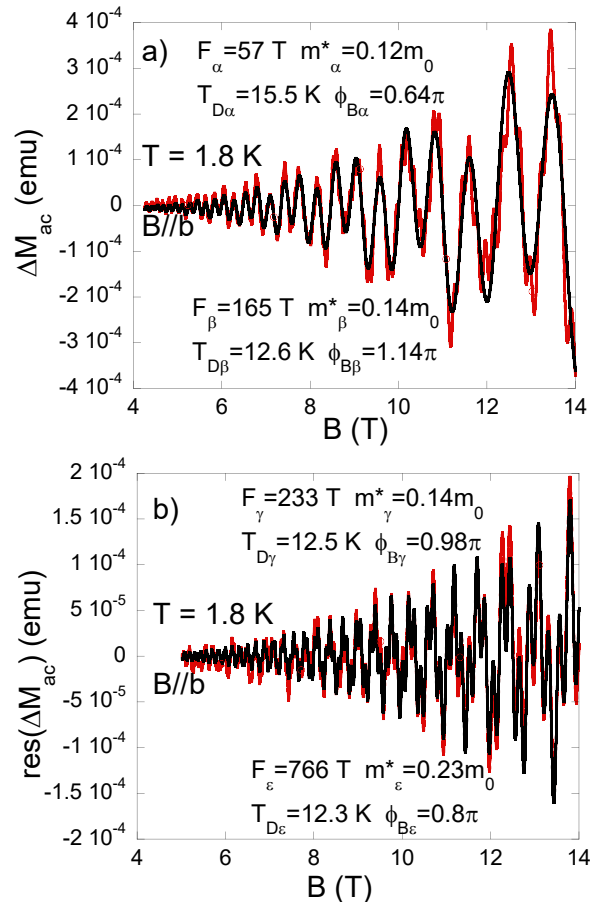


Figure 2. a) The oscillatory component of the isothermal magnetization  $\Delta M$  after subtracting a diamagnetic background for layered TaNiTe<sub>5</sub> at  $T = 1.8\text{K}$ . The magnetic field is applied parallel to the crystallographic *b* axis. The black lines show the fit of the oscillation pattern to the generalized two-band for the frequencies 56T and 165T. b) Two-band LK formula fit to the residual after subtracting the fit curve of a) from the oscillatory components. The data and fit within the magnetic field range, clearly shows that the data can be best fitted by the four-band LK formula.

also include a phase shift  $\phi = \phi_B/2\pi + \delta$  where  $\phi_B$  is the Berry phase, and  $\delta$  is an additional phase shift depending on the dimensionality of the Fermi surfaces, i.e.,  $\delta = 0$  for 2D Fermi surfaces, and  $\delta = \pm 1/8$  for 3D Fermi surfaces ( $-1/8$  for the electron-like and  $1/8$  for the hole-like). The Dingle factor

$$R_D = \exp(-\pi/\omega_c \tau_S) = \exp(-\hbar k_F/2eBl) \quad (2)$$

describes the increase in damping as the orbitally

averaged mean free path  $\ell$  decreases. It also depends on the average Fermi wave vector  $k_F$  of the orbit, where  $T_D$  is the Dingle temperature,  $\tau_S$  is the scattering time, and  $k_B$  is the Boltzmann constant.

Equipped with this formalism, we will illustrate our analysis based on the data obtained from magnetization measurements with the magnetic field applied along the crystallographic  $b$  axis. Analysis for  $\mathbf{B} \parallel a$  and  $\mathbf{B} \parallel c$  follows analogously. From the magnetic field sweeps at various temperatures we can perform polynomial background subtraction, fast Fourier transform, and extract the effective mass  $m^*$  using Equation 1 (see Figure 8 and Figure 9 in the appendix). With the fitted effective mass as a known parameter, we have further fitted the oscillation pattern at 1.8K, represented by the red line in Figure 2 a), to the LK formula, from which the Dingle temperature  $T_D$ , quantum mobility  $\mu_q$ , and the Berry phase  $\phi_B$  of the Fermi pockets are extracted and listed in Table I. Here, the black lines show the fit of the generalized two-band LK formula to the oscillation pattern for the frequencies  $F_\alpha=57\text{T}$  and  $F_\beta=165\text{T}$ . After subtracting this oscillation pattern, we performed another two-band LK formula fit to the residual data as shown in Figure 2 b). We conclude that the data can best be fitted by the four-band LK formula. Our analysis indicates that the extracted values of Berry phase for the obtained Fermi pockets for  $\delta = 0$  are close to  $\pi$  suggesting nontrivial topological properties of layered TaNiTe<sub>5</sub>. The fitted Dingle temperature  $T_D$ , corresponding to the quantum relaxation time  $\tau_q = \hbar/(4\pi^2 k_B T_D)$  and quantum mobility  $\mu_q = e\tau_q/(m^* m_e)$  ( $m_e$  being the electron mass) for all four pockets are also summarized in Table I. Furthermore, the mean free path  $l$  can be approximated under the assumption of a spherical Fermi surface:

$$l = \frac{\sqrt{2e\hbar^3 F}}{2\pi m^* m_e k_B T_D} \quad (3)$$

Based on the extracted oscillation frequencies, effective masses, and Dingle temperatures, we can characterise the observed Fermi surfaces in TaNiTe<sub>5</sub>. A similar analysis of the measured magnetization data at the same temperatures was performed for  $\mathbf{B} \parallel a$  and  $\mathbf{B} \parallel c$ , and the extracted parameters of the LK fitting are provided in the appendix in Figure 16. Note, that for  $\mathbf{B} \parallel c$  the amplitude was too low to obtain reliable values for

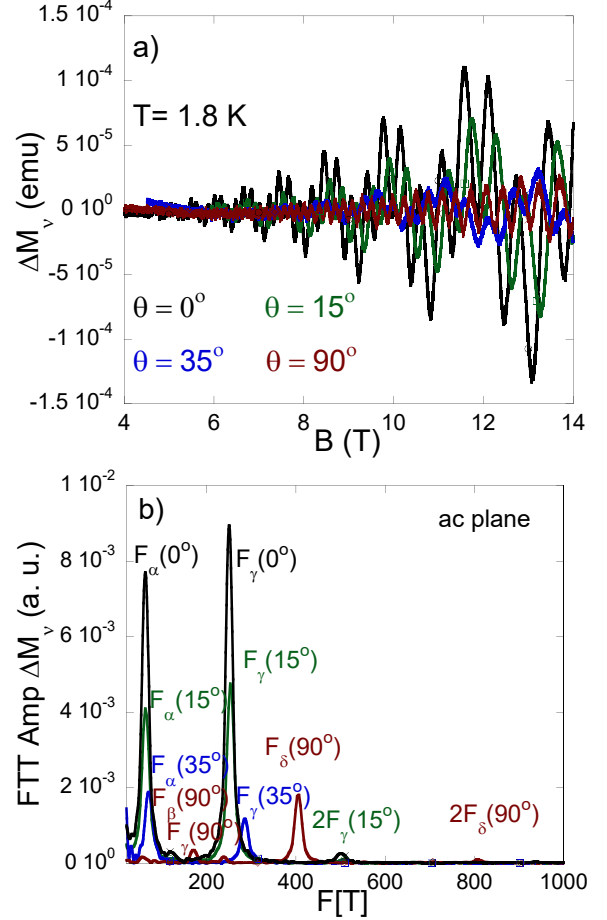


Figure 3. a) The magnetic field-dependent oscillatory components of the magnetization after subtracting the linear diamagnetic background at different angles in the  $a$ - $c$  plane at  $T = 1.8\text{K}$ . b) The corresponding FFT spectra for different angles. The angle  $\theta$  in the  $a$ - $c$  plane is defined as the angle between the applied magnetic field and the  $a$  axis.

the Berry phase  $\Phi_B$  for  $\alpha$  and  $\gamma$ .

To probe the morphology of the Fermi surface, we also carried out angle-dependent quantum oscillation measurements with the applied magnetic field in the  $a$ - $c$  plane. The dHvA oscillations in the angle range from  $0^\circ$  to  $90^\circ$  at  $T = 1.8\text{K}$  are plotted in Figure 3 a), where  $\theta$  is defined as the angle between the direction of magnetic field  $\mathbf{B}$  and the  $a$  axis. With increasing angle  $\theta$  from  $0^\circ$  to  $90^\circ$ , the oscillation components are suppressed gradually. The multi-periodic oscillation patterns can be observed at all angles from  $0^\circ$  to  $90^\circ$ , demonstrat-

Table I. Extracted properties from de Haas van Alphen oscillations in the magnetization.

	F (T)	$A_F$ ( $\text{\AA}^{-2}$ )	$m^*$ ( $m_e$ )	$T_D$ (K)	$\tau_q$ ( $10^{-14}$ s)	$\mu_q$ ( $\text{m}^2/\text{Vs}$ )	$l$ (nm)	$\phi_B$ ( $\pi$ )
$B \parallel b$								
$\alpha$	56.8(3)	0.00542(3)	0.12(1)	15.5(3)	7.8(2)	0.11(1)	31(3)	0.64(5)
$\beta$	164.7(3)	0.01572(3)	0.14(1)	12.6(3)	9.6(2)	0.121(9)	56(4)	1.14(4)
$\gamma$	233.1(3)	0.02225(3)	0.14(2)	12.5(5)	9.7(4)	0.12(2)	70(10)	0.98(3)
$\varepsilon$	766.0(5)	0.07312(5)	0.23(2)	12.3(5)	9.9(4)	0.076(7)	76(7)	0.81(4)
$B \parallel c$								
$\alpha$	55.3(3)	0.00528(3)	0.17(2)	28.6(3)	4.25(4)	0.044(5)	12(1)	-
$\beta$	173.8(4)	0.01659(4)	0.20(2)	13.4(3)	9.1(2)	0.080(8)	38(4)	1.03(3)
$\gamma$	240.0(4)	0.02291(4)	0.24(3)	13.6(4)	8.9(3)	0.066(8)	37(5)	-
$\delta$	405.2(4)	0.03868(4)	0.41(2)	4.7(3)	26(2)	0.111(9)	81(7)	1.30(3)
$B \parallel a$								
$\alpha$	63.0(3)	0.00601(3)	0.13(1)	15.8(3)	7.7(1)	0.104(8)	30(2)	1.10(5)
$\gamma$	251.0(4)	0.02396(4)	0.16(1)	10.8(3)	11.3(3)	0.124(8)	71(5)	1.01(5)
$B \parallel a \rightarrow B \parallel c$ ( $\theta = 15^\circ$ )								
$\alpha$	64.0(2)	0.00611(2)	0.19(1)	12.9(5)	9.4(4)	0.087(6)	25(2)	0.62(3)
$\gamma$	254.0(4)	0.02425(4)	0.24(1)	8.7(3)	14.0(5)	0.102(6)	59(3)	0.95(4)
$B \parallel a \rightarrow B \parallel c$ ( $\theta = 35^\circ$ )								
$\alpha$	73.0(2)	0.00697(2)	0.18(1)	12.4(4)	9.8(3)	0.096(6)	30(2)	0.61(3)
$\gamma$	286.0(4)	0.02730(4)	0.26(1)	12.5(4)	9.7(3)	0.066(3)	40(2)	1.28(5)

Table II. Extracted properties from Shubnikov de Haas oscillations in the resistivity with  $B \parallel b$  and  $I \parallel a$ .

	F (T)	$A_F$ ( $\text{\AA}^{-2}$ )	$m^*$ ( $m_e$ )	$T_D$ (K)	$\tau_q$ ( $10^{-14}$ s)	$\mu_q$ ( $\text{m}^2/\text{Vs}$ )	$l$ (nm)	$\phi_B$ ( $\pi$ )
$\alpha$	53.0(3)	0.00506(3)	0.14(2)	12.9(4)	9.4(3)	0.12(2)	31(5)	1.03(3)
$\beta$	163.0(4)	0.01556(4)	0.23(1)	14.7(3)	8.3(2)	0.063(3)	29(1)	1.05(4)
$\gamma$	233(3)	0.0222(3)	0.23(3)	-	-	-	-	-
$\varepsilon$	766(5)	-	-	-	-	-	-	-

ing the 3D character of the Fermi surface. Figure 3 b) shows the corresponding FFT spectra for each angle  $\theta$ . It can be seen that with increasing the angle  $\theta$  the oscillation frequency  $F_\alpha$  changes only slightly from 63T ( $\theta = 0^\circ$ ) to 73T ( $\theta = 35^\circ$ ), and then to 55T ( $\theta = 90^\circ$ ) indicating a nearly spherical Fermi pocket. On the other hand,  $F_\gamma$  increases from 251T ( $\theta = 0^\circ$ ) to 286T ( $\theta = 35^\circ$ ), and then decreases to 240T ( $\theta = 90^\circ$ ) indicating 3D elliptical Fermi pocket. Both Fermi pockets can be observed in all directions of the magnetic field to the crystallographic axes, demonstrating the 3D character of these Fermi surfaces. Chen et al. [23] reported that the angle dependence of  $F_\beta$  can well be fitted

with the 3D ellipsoid model, implying that the  $\beta$  band has an anisotropic 3D Fermi surface. The morphology of  $\varepsilon$  and  $\delta$  bands is difficult to extract, and further investigation at high fields is required.

The rotation study was performed in the temperature range from 1.8K to 22K, and the masses and other temperature dependent parameters were also extracted and listed in Table I.

## B. Magnetoresistance

Figure 4 a) shows the magnetoresistance data with the magnetic field parallel to the  $b$  axis and

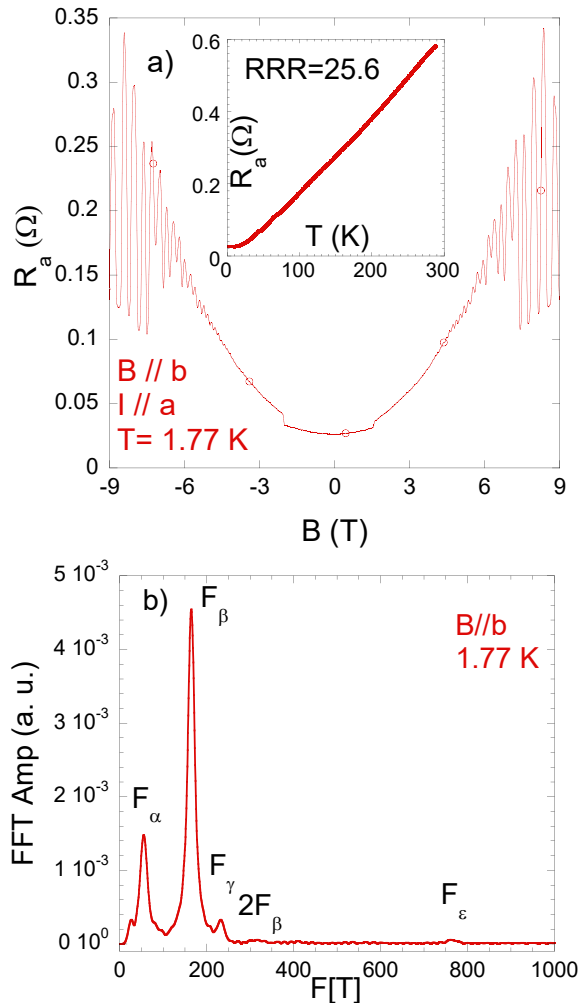


Figure 4. a) Magnetic field dependent resistance  $R_a$  with the current applied along the  $a$  axis, and the magnetic field parallel to the  $b$  axis. The inset shows the temperature dependence of the resistance  $R_a$  at 0T. b) The FFT spectrum of  $\Delta R_a$  generated in the magnetic field range from 3 to 9T.

the applied current parallel to the  $a$  axis. The magnetoresistance  $R_a$  shows very strong quantum oscillations at magnetic fields above 3T, indicating possible linear band dispersions close to the Fermi level and a high-quality of this single crystal. This result is in contrast to recent works [22, 23], in which quantum oscillations in the magnetoresistance of  $\text{TaNiTe}_5$  were only measured at much higher magnetic fields. The inset to Figure 4 a) shows the temperature dependence of the resis-

tance  $R_a$  displaying a typical metallic behaviour. The resistance follows a  $T$ -linear dependence from 280K to 60K and then a cross-over to a quadratic  $T$  dependence indicating Fermi liquid behaviour below 50K. The residual resistance ratio of  $\text{RRR} = 25.6$  is measured. We have performed a fast Fourier transform of the isothermal magnetoresistance sweep data shown in Figure 4 a). Figure 4 b) shows the FFT amplitude of the spectrum that has been generated from the magnetoresistance data in the magnetic field range between 3 and 9T.

In Figure 4 b), five clearly resolved peaks are visible. The two largest amplitude peaks at 53T and 163T are labeled as  $F_\alpha$  and  $F_\beta$ , respectively. Three other peaks are identified as  $F_\gamma = 233$  T,  $F_\epsilon = 766$  T, and the second harmonic  $2F_\beta = 310$  T.  $F_\alpha$  and  $F_\beta$  were reported previously [22, 23]. Similar to the magnetization data, magnetoresistance data in the temperature range 1.77 - 20K for  $B \parallel b$  with the current in  $I \parallel a$  allows us to extract the effective mass. Given  $m^*$ , the Dingle temperature  $T_D$ , quantum mobility  $\mu_q$ , and the Berry phase  $\phi_B$  of the Fermi pockets are extracted at  $T = 1.77$ K, which is summarized Table II and visualized in Figure 14 a). The resolution of the  $\gamma$  and  $\epsilon$  bands is too low to extract most parameters other than the frequencies, and the effective mass for the  $\gamma$  band.

#### IV. AB INITIO CALCULATIONS

To gain further insight into the electronic structure of  $\text{TaNiTe}_5$ , we have performed density functional theory (DFT) calculations using the full-potential linearized augmented plane wave method implemented in the Wien2k package [27]. The PBE-GGA exchange-correlation functional [28] was chosen here. Calculations in the Brillouin zone were performed on a  $34 \times 34 \times 8$  k-point mesh. After the first run, we performed a force optimization on the internal positions and charge densities, after which we then included spin-orbit coupling (SOC).

The DFT calculated Fermi sheets of  $\text{TaNiTe}_5$  and respective electronic bands are shown in Figure 5. The electronic band structure of  $\text{TaNiTe}_5$  along the high-symmetry directions including spin-orbit coupling (SOC) is consistent with band structure calculations from the literature [21, 22, 29, 30]. From Figure 5 it can be seen that linearly dispersing bands appear in pairs along the A-Z-R high-symmetry line, forming Type-I Dirac cones in

point Z, and Type-II Dirac cones in point R with linear dispersion as the bands maintain their spin-degeneracy. Similar to the quasi-one-dimensional family members TaXTe<sub>5</sub> (X = Pd, Pt), TaNiTe<sub>5</sub> also hosts cubic Dirac crossing along the symmetry line Z-T, which connect to quasi-linear band crossings along  $\Gamma$ -Z and T-Y [22, 31, 32].

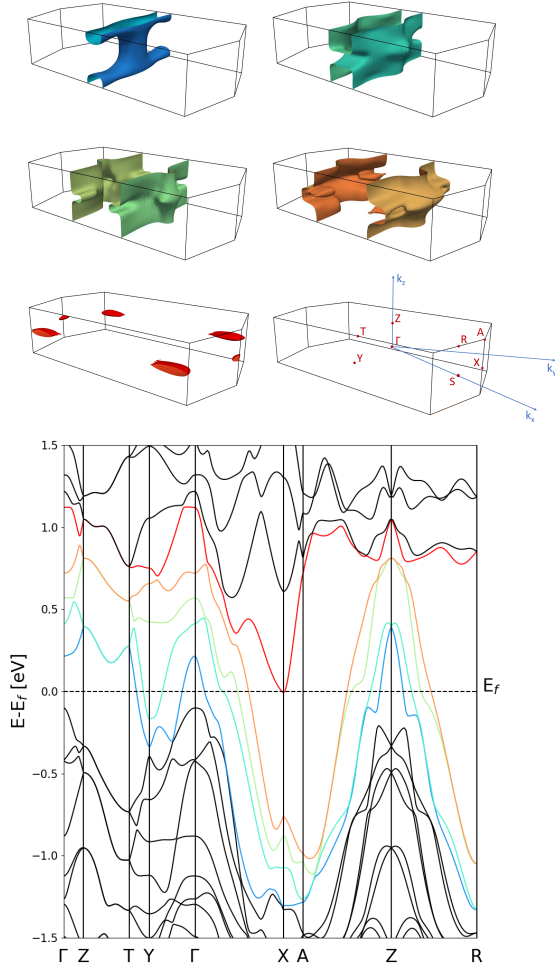


Figure 5. Density functional theory (DFT) calculated populated Fermi surfaces of TaNiTe<sub>5</sub> arising from five bands that cross the Fermi energy. Below is the electronic band structure of TaNiTe<sub>5</sub> along high-symmetry directions including spin-orbit coupling (SOC), where the five bands crossing the Fermi level are highlighted in color to match the Fermi sheets above.

## V. CONCLUSIONS

In summary, we have performed high-resolution measurements of de-Haas-van-Alphen and Shubnikov-de-Haas quantum oscillations in layered TaNiTe<sub>5</sub> by extending the magnetic field range up to 14T for all three crystallographic axes. The obtained fundamental frequencies in the FFT spectra resulting from dHvA measurements are consistent with those found in SdH measurements when the magnetic field is applied parallel to the *b* axis. Furthermore, we discovered the new frequency  $F_\delta=405\text{T}$  for  $\mathbf{B} \parallel c$  that has been absent from the literature thus far. Lifshitz-Kosevich fitting revealed that the main oscillations are in fact composed of at least three quasi-three-dimensional  $F_\alpha$ ,  $F_\beta$  and  $F_\gamma$  Fermi surface bands, which we attribute to the nontrivial Dirac Fermi surface pockets. The morphology of the  $\delta$  and  $\varepsilon$  bands is difficult to extract, and further investigation in high magnetic fields is required. Our results and interpretation imply that the quasiparticle properties of layered TaNiTe<sub>5</sub> are topologically nontrivial at low temperatures.

## ACKNOWLEDGMENTS

This work was supported by the Croatian Science Foundation under the project IP 2018 01 8912 and by the EPSRC of the UK under grant EP/X011992/1. This work was also supported by the Henry Royce Institute for advanced materials through the Equipment Access Scheme enabling access to the Magnetic Property Measurement System (MPMS) at Cambridge; Cambridge Royce facilities grant EP/P024947/1 and Sir Henry Royce Institute - recurrent grant EP/R00661X/1)

- 
- [1] S. M. Young and C. L. Kane, *Phys. Rev. Lett.* **115**, 126803 (2015).
- [2] M. Yan, H. Huang, K. Zhang, E. Wang, W. Yao, K. Deng, G. Wan, H. Zhang, M. Arita, H. Yang, Z. Sun, H. Yao, Y. Wu, S. Fan, W. Duan, and S. Zhou, *Nat. Commun.* **8**, 257 (2017).
- [3] J. Xiong, S. K. Kushwaha, T. Liang, J. W. Krizan, M. Hirschberger, W. Wang, R. J. Cava, and N. P. Ong, *Science* **350**, 413 (2015).
- [4] S. Borisenko, Q. Gibson, D. Evtushinsky, V. Zabolotnyy, B. Buchner, and R. J. Cava, *Phys. Rev. Lett.* **113**, 027603 (2014).
- [5] S. M. Huang, S. Y. Xu, I. Belopolski, C. C. Lee, G. Chang, B. Wang, N. Alidoust, G. Bian, M. Neupane, C. Zhang, S. Jia, A. Bansil, H. Lin, and M. Z. Hasan, *Nat. Commun.* **6**, 7373 (2015).
- [6] A. A. Soluyanov, D. Gresch, Z. Wang, Q. Wu, M. Troyer, X. Dai, and B. A. Bernevig, *Nature (London)* **527**, 495 (2015).
- [7] H. Weng, C. Fang, Z. Fang, B. A. Bernevig, and X. Dai, *Phys. Rev. X* **5**, 011029 (2015).
- [8] B. Q. Lv, N. Xu, H. M. Weng, J. Z. Ma, P. Richard, X. C. Huang, L. X. Zhao, G. F. Chen, C. E. Matt, F. Bisti, V. N. Strocov, J. Mesot, Z. Fang, X. Dai, T. Qian, M. Shi, and H. Ding, *Nat. Phys.* **11**, 724 (2015).
- [9] S.-Y. Xu, N. Alidoust, I. Belopolski, Z. Yuan, G. Bian, T.-R. Chang, H. Zheng, V. N. Strocov, D. S. Sanchez, G. Chang, *et al.*, *Nature Physics* **11**, 748 (2015).
- [10] S.-Y. Xu, I. Belopolski, N. Alidoust, M. Neupane, G. Bian, C. Zhang, R. Sankar, G. Chang, Z. Yuan, C.-C. Lee, *et al.*, *Science* **349**, 613 (2015).
- [11] S.-Y. Xu, C. Liu, S. K. Kushwaha, R. Sankar, J. W. Krizan, I. Belopolski, M. Neupane, G. Bian, N. Alidoust, T.-R. Chang, H.-T. Jeng, C.-Y. Huang, W.-F. Tsai, H. Lin, P. P. Shibayev, F.-C. Chou, R. J. Cava, and M. Z. Hasan, *Science* **347**, 294 (2015).
- [12] L. X. Yang, Z. K. Liu, Y. Sun, H. Peng, H. F. Yang, T. Zhang, B. Zhou, Y. Zhang, Y. F. Guo, M. Rahn, D. Prabhakaran, Z. Hussain, S. K. Mo, C. Felser, B. Yan, and Y. L. Chen, *Nat. Phys.* **11**, 728 (2015).
- [13] Z. K. Liu, L. X. Yang, Y. Sun, T. Zhang, H. Peng, H. F. Yang, C. Chen, Y. Zhang, Y. F. Guo, D. Prabhakaran, M. Schmidt, Z. Hussain, S. K. Mo, C. Felser, B. Yan, and Y. L. Chen, *Nat. Mater.* **15**, 27 (2016).
- [14] C. Fang, H. Weng, X. Dai, and Z. Fang, *Chin. Phys. B* **25**, 117106 (2016).
- [15] R. Yu, Z. Fang, X. Dai, and H. Weng, *Front. Phys.* **12**, 127202 (2017).
- [16] L. M. Schoop, M. N. Ali, C. Strasser, A. Topp, A. Varykhalov, D. Marchenko, V. Duppel, S. S. Parkin, B. V. Lotsch, and C. R. Ast, *Nat. Commun.* **7**, 11696 (2016).
- [17] C. Fang, Y. Chen, H.-Y. Kee, and L. Fu, *Phys. Rev. B* **92**, 081201(R) (2015).
- [18] T. Bzdusek, Q. Wu, A. Ruegg, M. Sigrist, and A. A. Soluyanov, *Nature (London)* **538**, 75 (2016).
- [19] S.-Y. Yang, H. Yang, E. Derunova, S. S. P. Parkin, B. Yan, and M. N. Ali, *Adv. Phys.: X* **3**, 1414631 (2018).
- [20] J. Hu, Z. Tang, J. Liu, X. Liu, Y. Zhu, D. Graf, K. Myhro, S. Tran, C. N. Lau, J. Wei, and Z. Mao, *Phys. Rev. Lett.* **117**, 016602 (2016).
- [21] Z. Hao, W. Chen, Y. Wang, J. Li, X.-M. Ma, Y.-J. Hao, R. Lu, Z. Shen, Z. Jiang, W. Liu, Q. Jiang, Y. Yang, X. Lei, L. Wang, Y. Fu, L. Zhou, L. Huang, Z. Liu, M. Ye, D. Shen, J. Mei, H. He, C. Liu, K. Deng, C. Liu, Q. Liu, and C. Chen, *Phys. Rev. B* **104**, 115158 (2021).
- [22] C. Xu, Y. Liu, P. Cai, B. Li, W. Jiao, Y. Li, J. Zhang, W. Zhou, B. Qian, X. Jiang, *et al.*, *The Journal of Physical Chemistry Letters* **11**, 7782 (2020).
- [23] Z. Chen, M. Wu, Y. Zhang, J. Zhang, Y. Nie, Y. Qin, Y. Han, C. Xi, S. Ma, X. Kan, J. Zhou, X. Yang, X. Zhu, W. Ning, and M. Tian, *Phys. Rev. B* **103**, 035105 (2021).
- [24] R. Ye, T. Gao, H. Li, X. Liang, and G. Cao, *AIP Advances* **12**, 045104 (2022).
- [25] C. E. W. Liimatta and J. A. Ibers, *J. Solid State Chem.* **78**, 7 (1989).
- [26] D. Shoenberg, (Cambridge Univ. Press, Cambridge, England, 1984).
- [27] P. Blaha, K. Schwarz, G. K. Madsen, D. Kvasnicka, J. Luitz, *et al.*, An augmented plane wave+ local orbitals program for calculating crystal properties **60** (2001).
- [28] J. P. Perdew, K. Burke, and M. Ernzerhof, *Phys. Rev. Lett.* **77**, 3865 (1996).
- [29] Y. Li, Z. Ran, C. Huang, G. Wang, P. Shen, H. Huang, C. Xu, Y. Liu, W. Jiao, W. Jiang, J. Hu, G. Zhu, C. Xu, Q. Lu, G. Wang, Q. Jing, S. Wang, Z. Shi, J. Jia, X. Xu, W. Zhang, W. Luo, and D. Qian, *Phys. Rev. Lett.* **128**, 106802 (2022).
- [30] D.-Y. Wang, Q. Jiang, K. Kuroda, K. Kawaguchi, A. Harasawa, K. Yaji, A. Ernst, H.-J. Qian, W.-J. Liu, H.-M. Zha, Z.-C. Jiang, N. Ma, H.-P. Mei, A. Li, T. Kondo, S. Qiao, and M. Ye, *Phys. Rev. Lett.* **129**, 146401 (2022).
- [31] W.-H. Jiao, X.-M. Xie, Y. Liu, X. Xu, B. Li, C.-Q. Xu, J.-Y. Liu, W. Zhou, Y.-K. Li, H.-Y. Yang, S. Jiang, Y. Luo, Z.-W. Zhu, and G.-H. Cao, *Phys.*

- Rev. B **102**, 075141 (2020).
- [32] W.-H. Jiao, S. Xiao, B. Li, C. Xu, X.-M. Xie, H.-Q. Qiu, X. Xu, Y. Liu, S.-J. Song, W. Zhou, H.-F. Zhai, X. Ke, S. He, and G.-H. Cao, Phys. Rev. B **103**, 125150 (2021).

## Appendix A: Methods

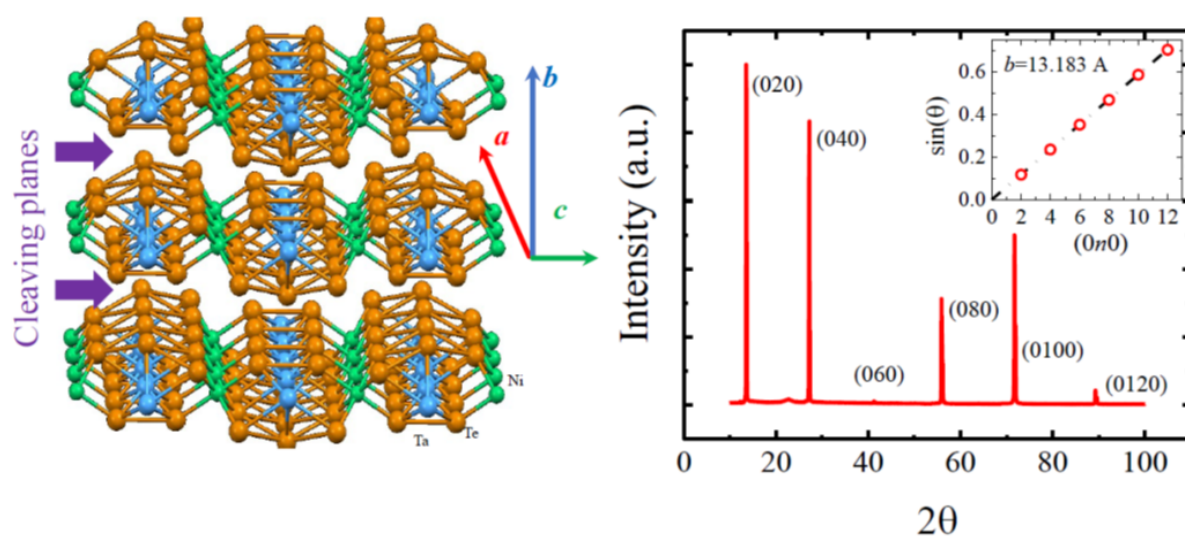


Figure 6. Left: Crystal structure of  $\text{TaNiTe}_5$  with 1D  $\text{NiTe}_2$  chains along the crystallographic  $a$ -axis. Right: Single crystal x-ray diffraction pattern. The inset shows the extracted value of the lattice parameter  $b$ . The sharp reflection peaks indicate the high quality of our crystals.

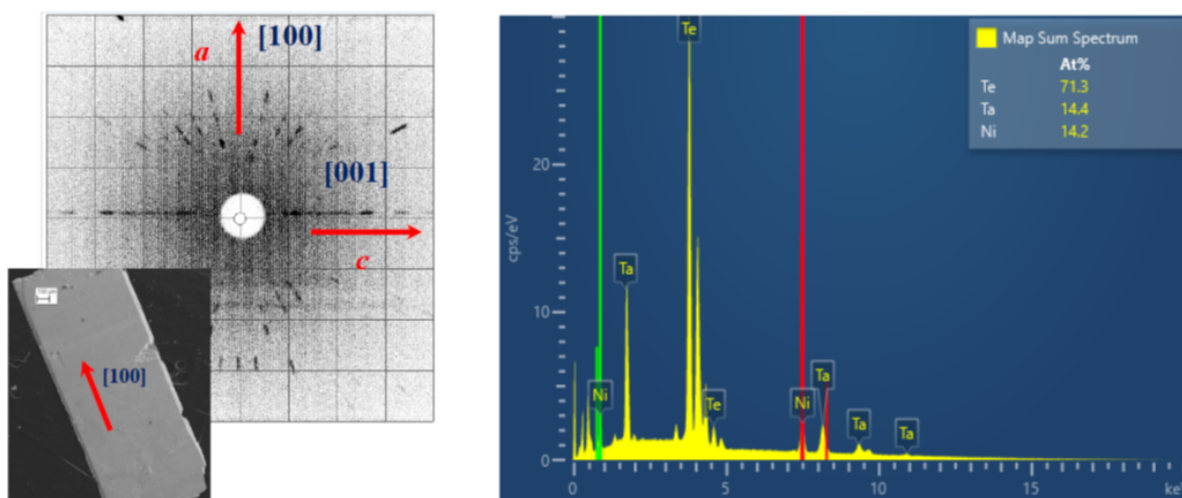


Figure 7. Laue x-ray diffraction pattern (left), and the energy-dispersive x-ray spectrum (right). The inset shows an optical image of a typical crystal.

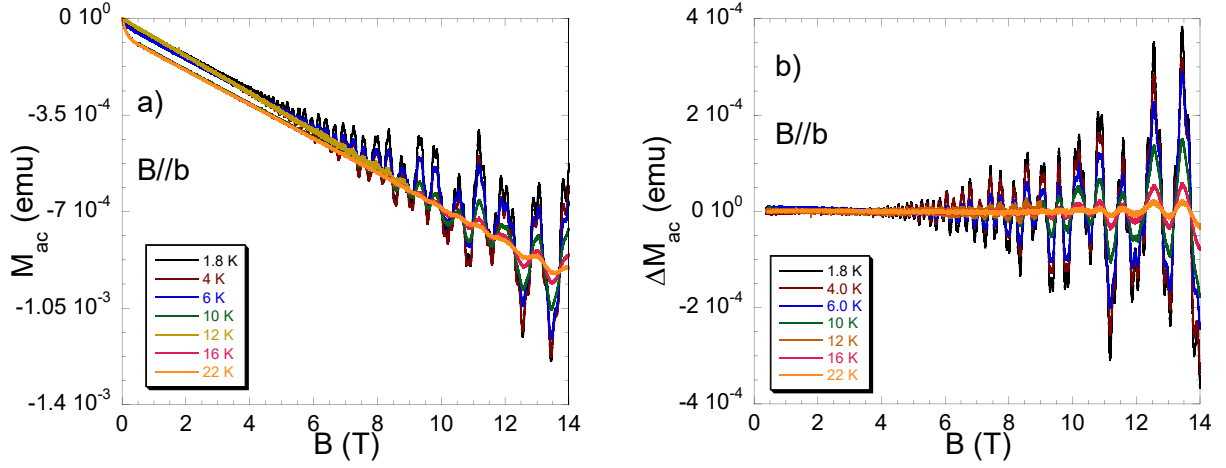
Appendix B: Magnetic field in  $B \parallel b$ 

Figure 8. a) The magnetic field sweeps of magnetization up to 14T on a layered TaNiTe<sub>5</sub> single crystal at various temperatures between 1.8K and 22K. The magnetic field is applied parallel to the crystallographic b axis. b) The oscillatory component of the isothermal magnetization  $\Delta M$  after subtracting the diamagnetic backgrounds at various temperatures from  $T = 1.8\text{K}$  to 22K.

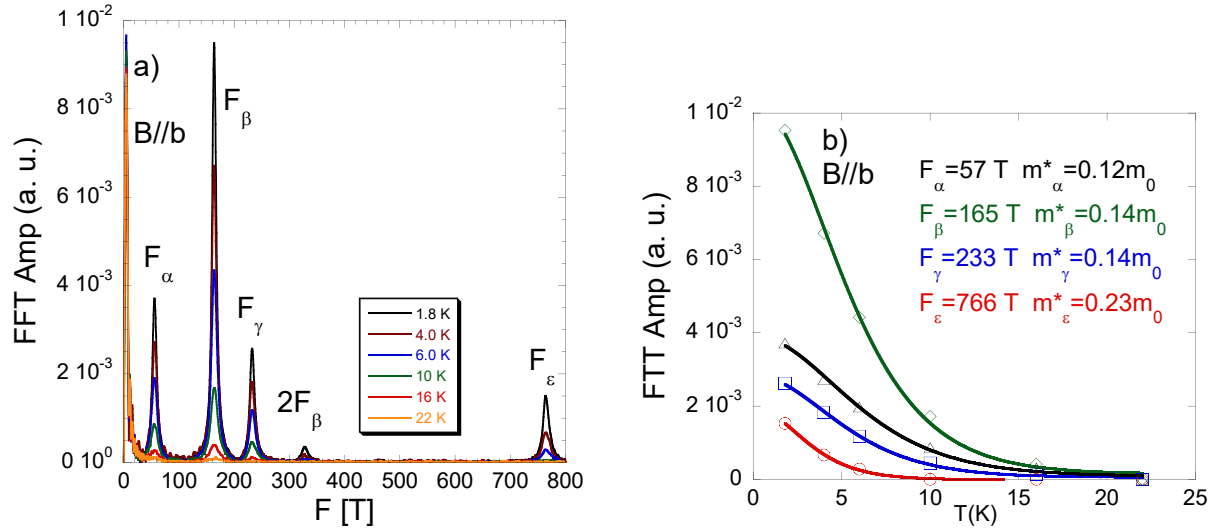


Figure 9. a) Analysis of the dHvA oscillations for  $B \parallel b$ . The FFT spectra of the oscillatory components of the dHvA oscillations for  $B \parallel b$  of the magnetization data at various temperatures. The FFT amplitude of the spectra has been generated from the data between 4T and 14T. b) The fits of the temperature damping factor  $R_T$  of the LK formula to the FFT amplitudes of the oscillatory components.

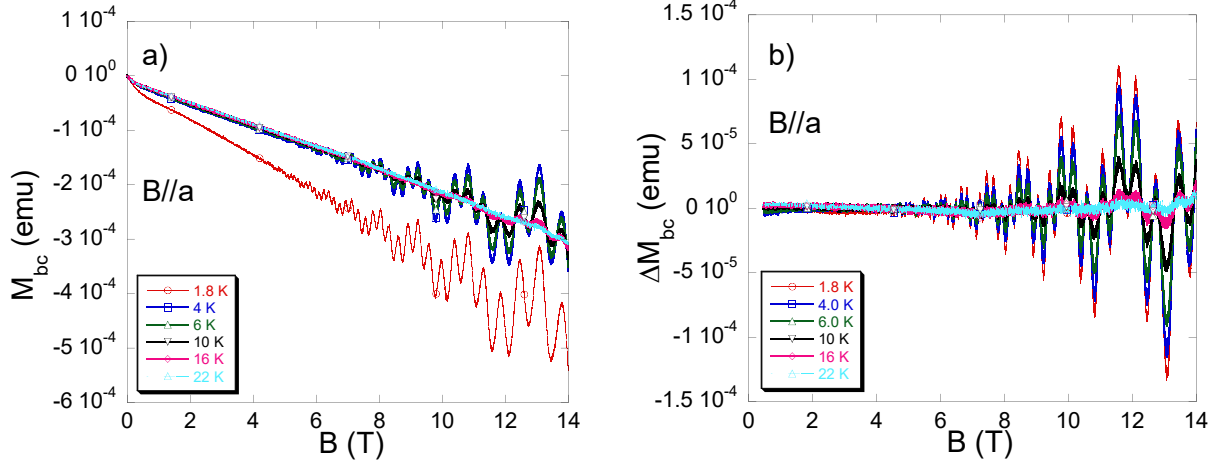
Appendix C: Magnetic field in  $B \parallel a$ 

Figure 10. a) The magnetic field sweeps of magnetization up to 14T on a layered  $\text{TaNiTe}_5$  single crystal at various temperatures between 1.8K and 22K. The magnetic field is applied parallel to the crystallographic  $a$  axis. b) The oscillatory component of the isothermal magnetization  $\Delta M$  after subtracting the diamagnetic backgrounds at various temperatures from  $T = 1.8\text{K}$  to 22K.

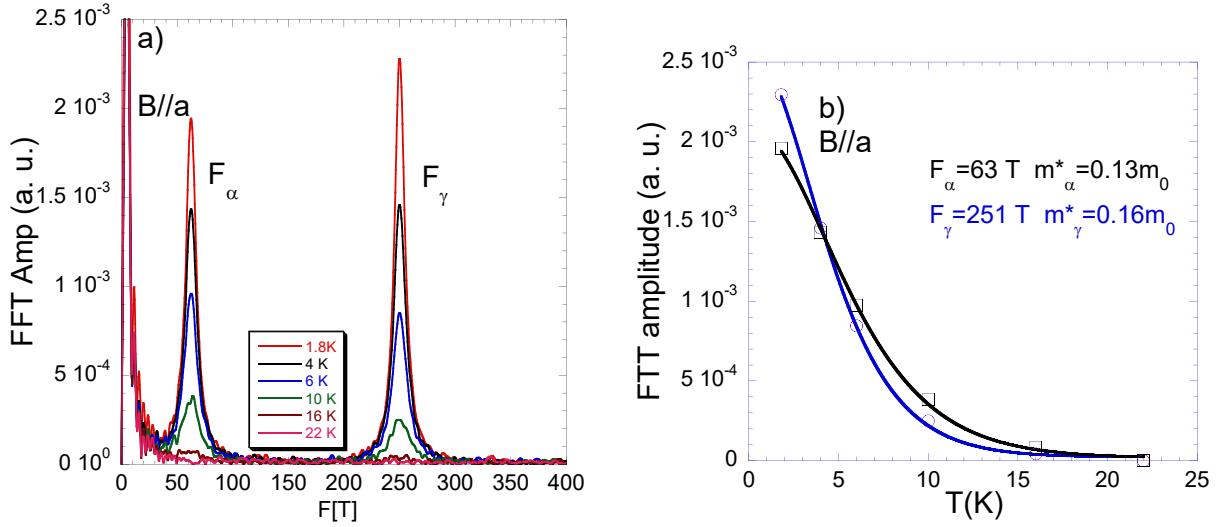


Figure 11. a) Analysis of the dHvA oscillations for  $B \parallel a$ . The FFT spectra of the oscillatory components of the dHvA oscillations for  $B \parallel a$  of the magnetization data at various temperatures. The FFT amplitude of the spectra has been generated from the data between 4T and 14T. b) The fits of the temperature damping factor  $R_T$  of the LK formula to the FFT amplitudes of the oscillatory components.

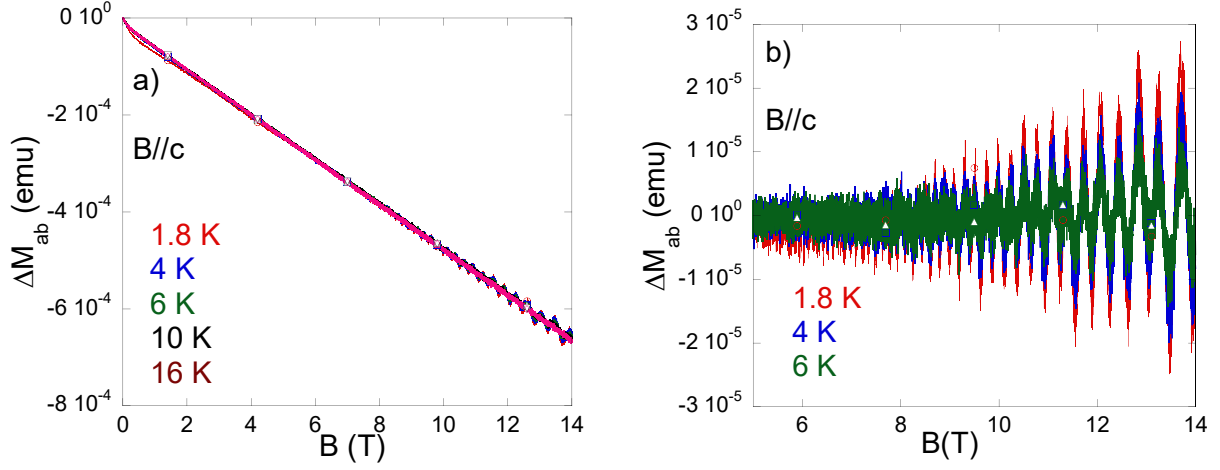
Appendix D: Magnetic field in  $B \parallel c$ 

Figure 12. a) The magnetic field sweeps of magnetization up to 14T on a layered  $\text{TaNiTe}_5$  single crystal at various temperatures between 1.8K and 16K. The magnetic field is applied parallel to the crystallographic  $c$  axis. b) The oscillatory component of the isothermal magnetization  $\Delta M$  after subtracting the diamagnetic backgrounds at various temperatures from  $T = 1.8\text{K}$  to 6K.

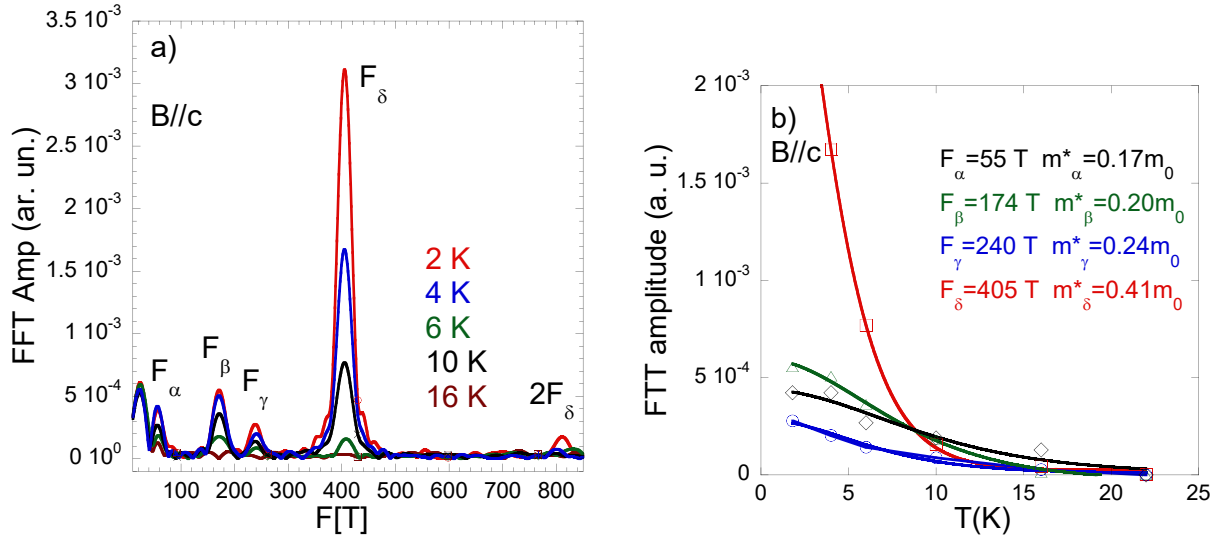


Figure 13. a) Analysis of the dHvA oscillations for  $B \parallel c$ . The FFT spectra of the oscillatory components of the dHvA oscillations for  $B \parallel c$  of the magnetization data at various temperatures. The FFT amplitude of the spectra has been generated from the data between 4T and 14T. b) The fits of the temperature damping factor  $R_T$  of the LK formula to the FFT amplitudes of the oscillatory components.

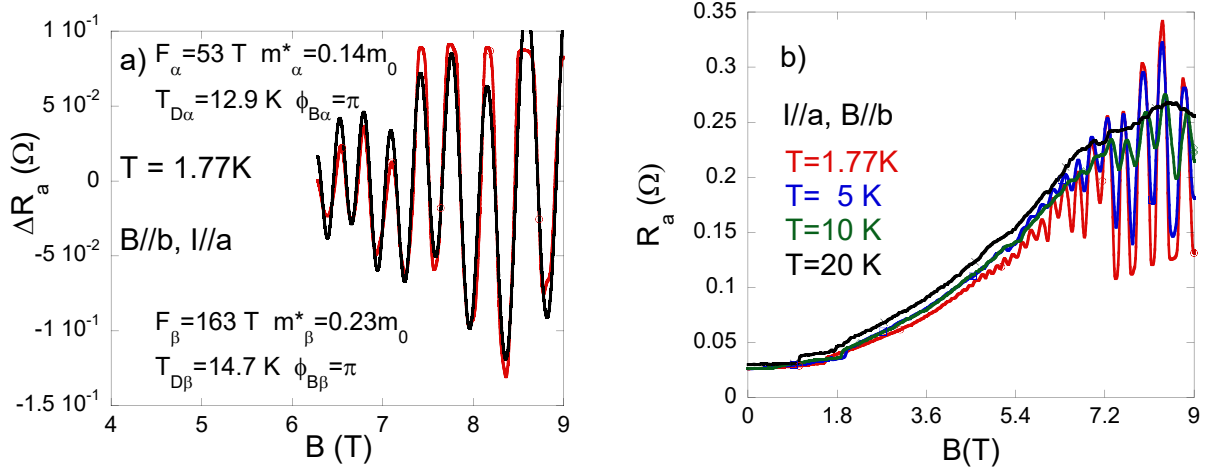
Appendix E: Resistance in  $B \parallel b$ 

Figure 14. a) The oscillatory component of the resistance after subtracting the background at  $T = 1.77\text{K}$  b) The magnetic field sweeps of resistance up to 9T on a layered TaNiTe<sub>5</sub> single crystal at various temperatures between 1.77K and 20K. The magnetic field is applied parallel to the crystallographic b axis.

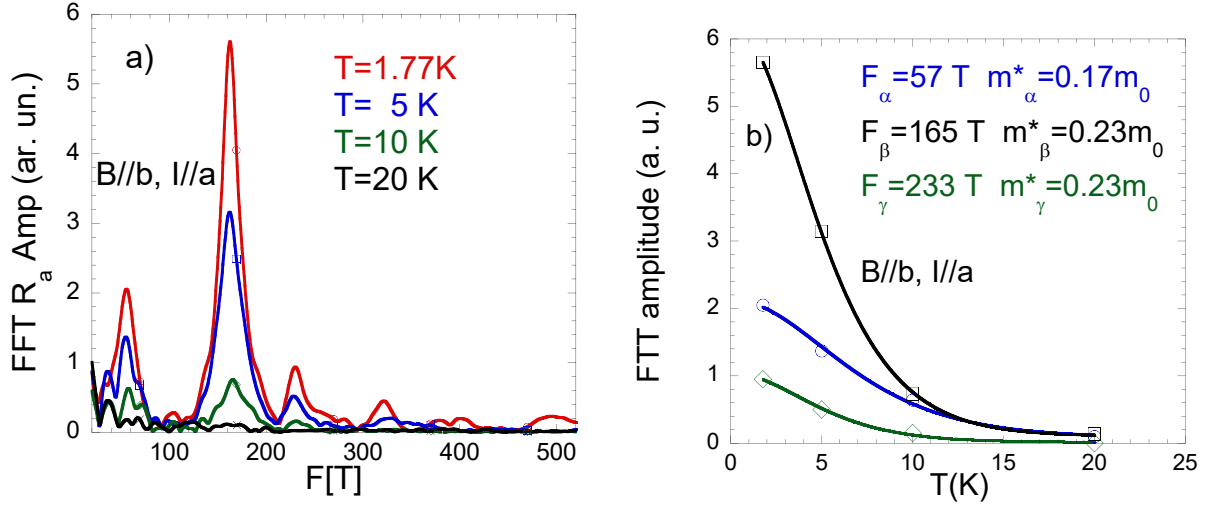


Figure 15. a) Analysis of the SdH oscillations for  $B \parallel b$ . The FFT spectra of the oscillatory components of the SdH oscillations for  $B \parallel b$  of the magnetoresistance data at various temperatures. The FFT amplitude of the spectra has been generated from the data between 6T and 9T. b) The fits of the temperature damping factor  $R_T$  of the LK formula to the FFT amplitudes of the oscillatory components.

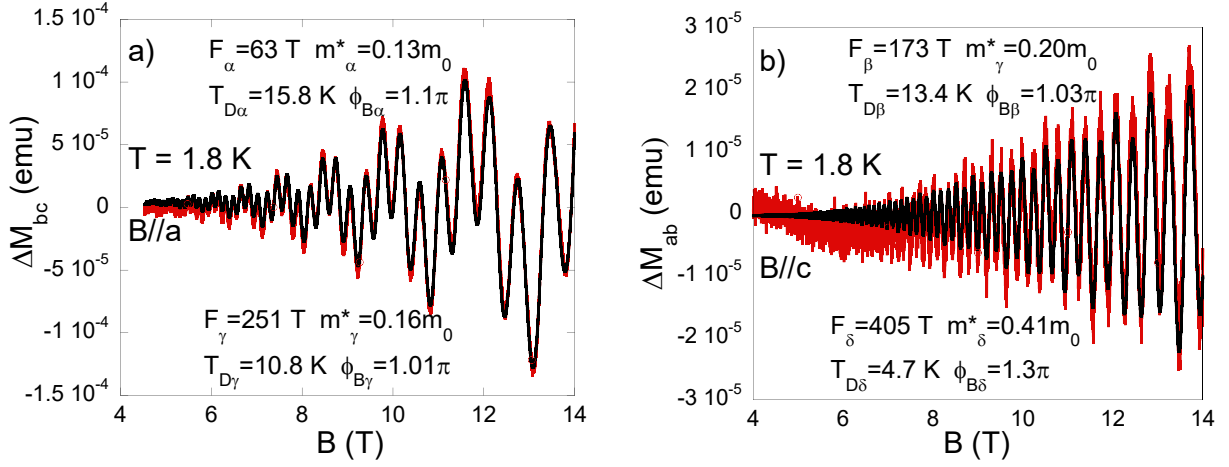


Figure 16. a, b) The oscillatory components of the isothermal magnetization  $\Delta M$  after subtracting a diamagnetic background for layered  $\text{TaNiTe}_5$  at  $T = 1.8 \text{ K}$ . The magnetic field is applied parallel to the crystallographic a, c axes, respectively. The black lines show the fit of the oscillation pattern to the generalized two-band for the frequencies 63T and 251T, and to the generalized four-band for the frequencies 55T, 173T, 240T and 405T. Note that the resolution of the data for  $B \parallel c$  was too low to extract meaningful information about the  $F_\gamma$  and  $F_\epsilon$  bands after subtracting the oscillations from the  $F_\beta$  and  $F_\delta$  bands